Journal of Solid State Electrochemistry (2019) 23:2737–2746
https://doi.org/10.1007/s10008-019-04364-9

ORIGINAL PAPER

A facile preparation of nano-$Ag_4Bi_2O_5/MnO_x$ on wrinkled rGO as greatly enhanced ternary catalyst for oxygen reduction reaction in alkaline electrolyte

Jing Wang[1] · Junqing Pan[1] · Xun Zeng[1] · Guangshi Tang[1] · Jiaqi Cai[1] · Abrar Khan[1] · Yanzhi Sun[1] · Xiaoguang Liu[1]

Received: 19 December 2018 / Revised: 6 August 2019 / Accepted: 7 August 2019 / Published online: 17 August 2019

Abstract

Nano-$Ag_4Bi_2O_5/MnO_x$@rGO ternary composite was prepared via a facile coprecipitation method in rGO dispersed concentrated KOH solution under precisely controlled conditions. Morphology characterizations indicate that the $Ag_4Bi_2O_5/MnO_x$ composite with corncob-like shape of 200 nm in length and 50 nm in width is loaded on the wrinkled rGO. The electrochemical tests find that the optimized ternary catalyst with 60% rGO contained offers much higher initial potential (0.0799 V vs. Hg/HgO) and limiting current density (6.164 mA cm^{-2}) than that of the standardized Pt/C (0.017 V and 5.09 mA cm^{-2}) at a rotation rate of 1600 rpm. Furthermore, the catalyst possesses preferable durability and anti-methanol as compared with Pt/C. The $Ag_4Bi_2O_5/MnO_x$/rGO with surperior ORR properties indicates that it will be a promising catalyst for oxygen reduction reaction in alkaline electrolyte.

Keywords Ternary catalyst · Oxygen reduction reaction · Silver bismuthate · Manganese dioxide · Alkaline electrolyte

Introduction

Recently, due to the overuse of fossil energy, energy dilemma and environmental issue have become serious increasingly. Hence, the seeking for new projects to deal with the increasingly strained energy dilemma has been one of the most pressing challenges [1–3]. The fuel cell has attracted broad attention as a new type of high-efficient power source because it not only converts chemical energy into electric energy directly but also breaks through the limitation of Carnot cycle thermal efficiency. Compared to the fast anode process on the hydrogen electrode, the slow cathode process of oxygen relates to the breaking of O=O and the four-electron reduction process [4–7]. It is urgent to develop efficient catalysts to enhance the speed of oxygen reduction reaction which has a slow kinetic process with the higher activation energy and to promote the efficiency and specific power of the fuel cell [8–12].

Although platinum catalyst exhibits unique electrochemical performance, the scarcity and high cost limit its large-scale commercialization so that it becomes research focus to develop and improve new platinum free electrocatalysts which can substitute for platinum-based catalysts [13–20]. Moreover, it is more significant to exploit new catalyst used in alkaline electrolyte rather than in acid electrolyte because alkaline electrolyte offers more gentle corrosion to most of the metal oxide contained in catalysts [21]. At present, some hot materials have been proposed and researched, such as metal carbonitride catalysts [22–24], metal nitride catalysts [25–27], and transition metal oxides catalysts (e.g., MnO_x) [28–33]. Manganese dioxide has aroused much interest as an alternative catalyst because of its low price, abundant resources, various valence states, and environmental friendliness [28]. Liu Jing et al. have synthesized different morphologies of Mn_3O_4 and the comparison of them shows that the Mn_3O_4 nanoflakes possess better overall performance ($v_{1/2}$ of 0.82 V vs. RHE and j of 0.45 mA) than the morphology of nanoparticles and nanorods [30]. Cheng Fangyi et al. found that the catalyst activity of ORR of MnO_2 followed the order

Electronic supplementary material The online version of this article (https://doi.org/10.1007/s10008-019-04364-9) contains supplementary material, which is available to authorized users.

✉ Junqing Pan
jqpan@mail.buct.edu.cn

[1] State Key Laboratory of Chemical Resource Engineering, Beijing Engineering Center for Hierarchical Catalysts, Beijing Advanced Innovation Center for Soft Matter Science and Engineering, College of Chemistry, Beijing University of Chemical Technology, Beijing 100029, China

of α- > β- > γ-MnO_2 and the MnO_2 nanowires @Ni nanoparticles compound exhibited great properties with v_0 of 0.08 V (vs. Ag/AgCl) and j of 33.5 mA mg^{-1} [31]. Hazarika et al. have prepared a material in which mesoporous cubical Mn_2O_3 loaded on an active carbon with good ORR properties, showing a limited current of 4.4 mA cm^{-2} with high initial potential at 1600 rpm [32]. Manganese dioxide-based catalysts have shown good electrocatalytic properties for reduction of oxygen via 4 electron reaction pathways, while manganese-based catalysts have the disadvantage of being easy to decay in characteristics and the pure structure has unsatisfactory property [34].

Hence, some new research has been investigated on the MnO_2 for improving its catalytic performance, and metal cations as dopants have been introduced to alleviate the instability of structure during charging and discharging processes [35–37]. Silver and silver-based catalysts have not only high electrochemical activity and good methanol resistance but also strong stability which can support MnO_2 to a certain extent [21, 38–41]. However, the inferior conductivity and dispersibility of nanometal oxide particles have become the bottleneck limiting their further application [42]. The reduced graphene oxide (rGO), especially the wrinkled rGO sheets with high electroconductivity and large surface area, provide numerous nucleation sites to restrain the growth of nanoparticles. The wrinkled rGO as the new carrier can combine with metal oxide to provide more active sites, which can significantly improve their electrical conductivity, accelerate charge transport, and further reduce the polarization of ORR process [43–51]. Here, we propose a new ternary catalyst, $Ag_4Bi_2O_5/MnO_x$ ($1 \le x \le 2$), grown on wrinkled rGO. It has remarkably enhanced performance and overcome the abovementioned drawbacks of simplex catalyst by means of its better natural dispersibility, improved electrical conductivity, and new synergistic effect.

Herein, rGO-supported nano-$Ag_4Bi_2O_5/MnO_x$ (rGO-AM) composite was prepared via a facile coprecipitation method in high concentration of KOH solution with rGO dispersed. The obtained material demonstrates the equivalent catalytic activity to that of commercial Pt/C, superior service life, and excellent anti-methanol performance, so that rGO-AM will be a promising catalyst in the application of fuel cells.

Experimental

Synthesis of $Ag_4Bi_2O_5/MnO_x$/rGO

Firstly, 0 mg, 0.69 mg, 1.5 mg, 2.5 mg, 4.2 mg, 6.3 mg, 9.4 mg, and 14.3 mg rGO were added into 8 vessels each containing 100 mL 6.5 M KOH, respectively. Subsequently, they were dispersed into 8 uniform solutions by ultrasonic for 2 h and labeled as a series of solution A. In regard to each proton of solution A, 1.15 g Ag_2O and 1.17 g Bi_2O_3 were reacted with 50 mL 2 M HNO_3 to form the acidic Ag^+–Bi^{3+} solution, labeled as solution B. Then the two solutions of A and B were dropped into a 250-mL flask, separately by two peristaltic pumps at a rate of 150 mL h^{-1} under 30 °C, meanwhile the mixture in the flask was stirred at 2000 rpm, and

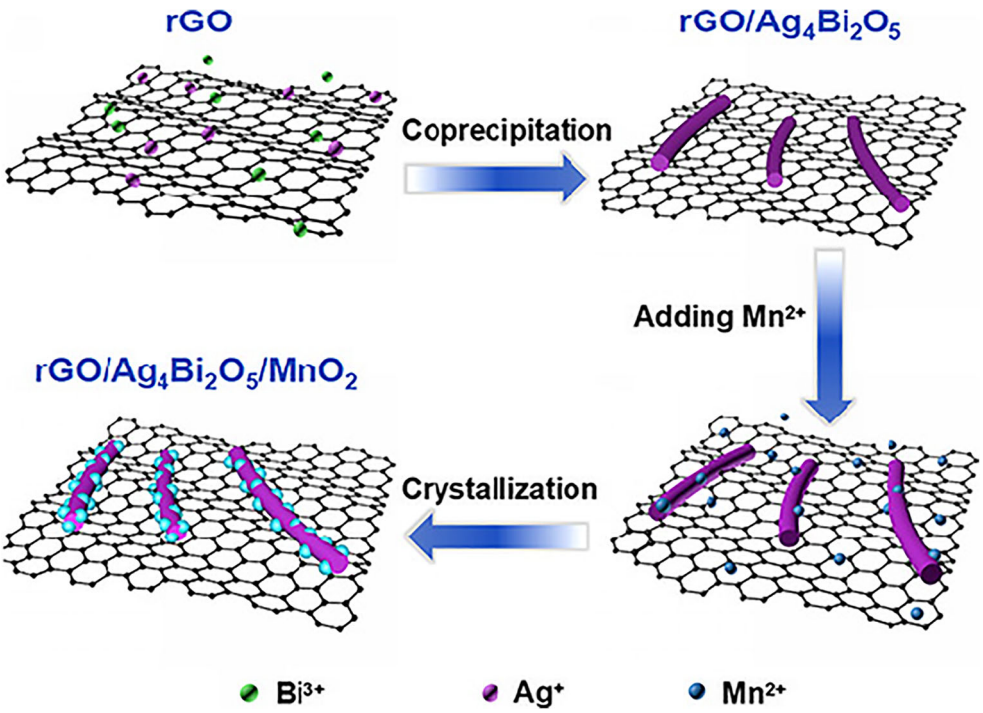

Fig. 1 Schematic diagram of the synthetic process of $Ag_4Bi_2O_5/MnO_x$/rGO

finally the mixed mother liquor was aged for 1 h. Then 1.0 mL 50% $Mn(NO_3)_2$ solution was diluted in deionized water to prepare 20 mL solution, marked as solution C. The solution C was pumped into the above mother liquor at a speed of 3 mL min^{-1} and the mixture was crystallized gradually for 2 h. The 8 portions of solution A were processed the same way as the above procedure. So, 8 crystallized samples were obtained. All the reagents and materials used were listed in Table S1. The schematic diagram of the synthetic process of $Ag_4Bi_2O_5/MnO_x$/rGO is displayed in Fig. 1.

The crystallized samples were pulpified with 100 mL DI water separately and filtrated until the pH of filt liquor < 8. The obtained solids were placed in a vacuum oven at 30 °C overnight. These products were denoted as 0% rGO-AM, 10% rGO-AM, 20% rGO-AM, 30% rGO-AM, 40% rGO-AM, 50% rGO-AM, 60% rGO-AM, and 70% rGO-AM, separately.

Physicochemical and electrochemical measurements

All the investigated materials were characterized by SEM, XRD, EDS, and XPS, and the related information was also displayed in Table S2.

A three-electrode system containing 0.1 M KOH as electrolyte saturated with O_2 or Ar was adopted as follows:

1. Working electrode: a glassy carbon electrode (GCE) coated with catalyst
2. Auxiliary electrode: a platinum wire
3. Reference electrode: a Hg/HgO electrode

In this research, the Hg/HgO electrode was employed in the same electrolyte as the working electrode for the electrochemical assessment, so the potential difference (Hg/HgO vs. RHE) is pH independent, and the relation is as follows:

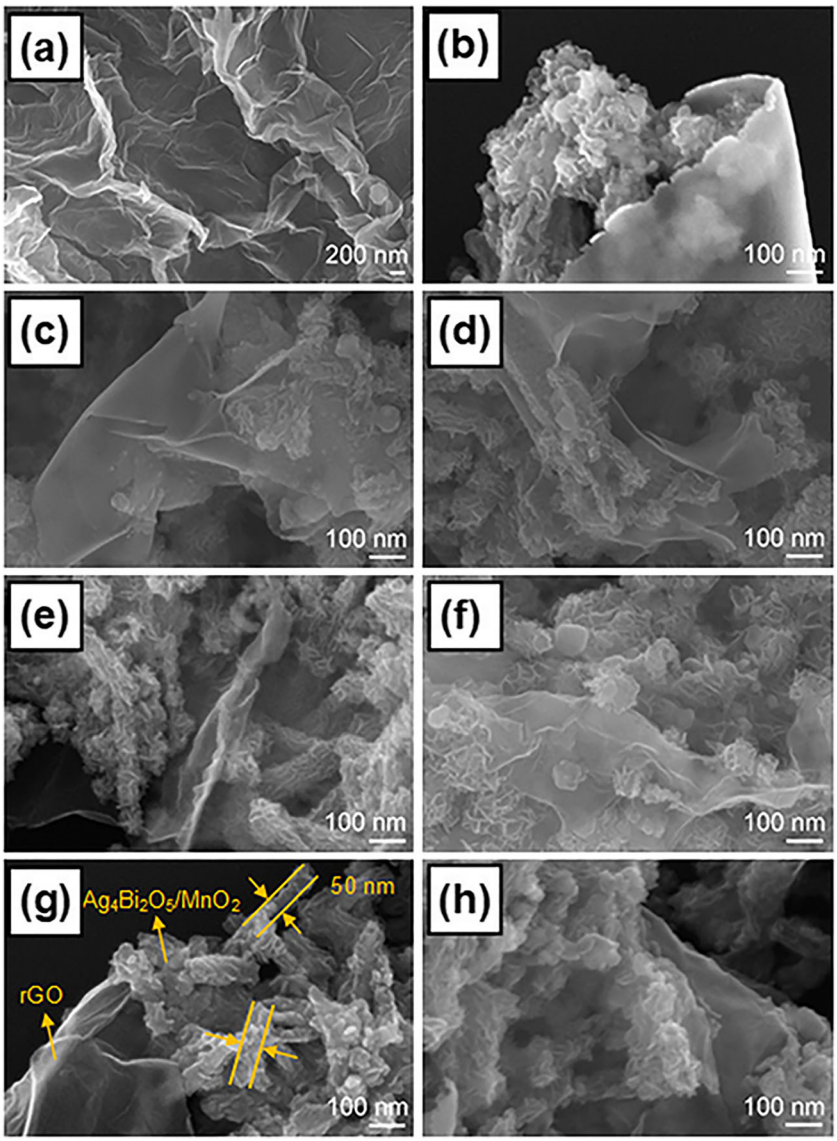

Fig. 2 SEM images of $Ag_4Bi_2O_5/MnO_x$/rGO with different contents of rGO: **a** pure rGO, **b** 10% rGO, **c** 20% rGO, **d** 30% rGO, **e** 40% rGO, **f** 50% rGO, **g** 60% rGO, **h** 70% rGO

E(RHE) = E(Hg/HgO) + 0.93 V

For preparation of a working electrode, the catalyst ink was firstly made up with the following components: 8 mg of the obtained materials as catalyst, 4 mg conductive graphite as conductive agent, 450 μL $(CH_3)_2CHOH$ and 630 μL DI water as dispersing agent, and 55 μL 5% Nafion solution as the raw material of proton exchange membrane which was formed after volatilization of solvent. The mixed catalyst ink was decentralized by ultrasonic for half hour to form a homogenous ink. Whereafter, 5.6 μL ink was applied on the glassy carbon electrode of 5 mm in diameter and solidified at 30 °C. The load amount of catalyst on the working electrodes was approximately 0.2 mg cm^{-2}. Both Pt/C and the obtained materials were prepared following the process and with the same load amount.

Before electrochemical tests, the electrolytes were aerated by O_2 or Ar for 30 min to ensure being saturated with the filled gas. Cyclic voltammetry (CV) of the catalyst electrode was carried out in the range from − 0.3 to 0.3 V (vs. Hg/HgO) with a scan rate of 50 mV s^{-1}. The linear sweep voltammetry (LSV) of the obtained rGO-AM catalysts was carried out on the rotating disk electrode at various rotation speeds of 400, 625, 900, 1225, 1600, 2025, 2500 rpm. The limiting current density (j) was read at − 0.30 V where the reaction was at equilibrium, the initial potential (v_0) was read as the current density was − 0.02 mA cm^{-2}, and every half-wave potential ($v_{1/2}$) value was read while the current density was half of the corresponding j. The i–t chronoamperometric test was performed in O_2 saturated 0.1 mol L^{-1} KOH solution at − 0.03 V for 10,800 s. The anti-methanol resistance was checked by chronoamperometric curves test at − 0.03 V for 2000 s in O_2 saturated 0.1 mol L^{-1} KOH solution, and 3.0 mol L^{-1} methanol provided at about 400 s during the test.

Results and discussion

Morphological and structural characterization

Figure 1 presents the schematic diagram of the synthesis process of AM-rGO composite, which undergoes two steps of co-precipitation in alkaline solution with rGO dispersion. As we

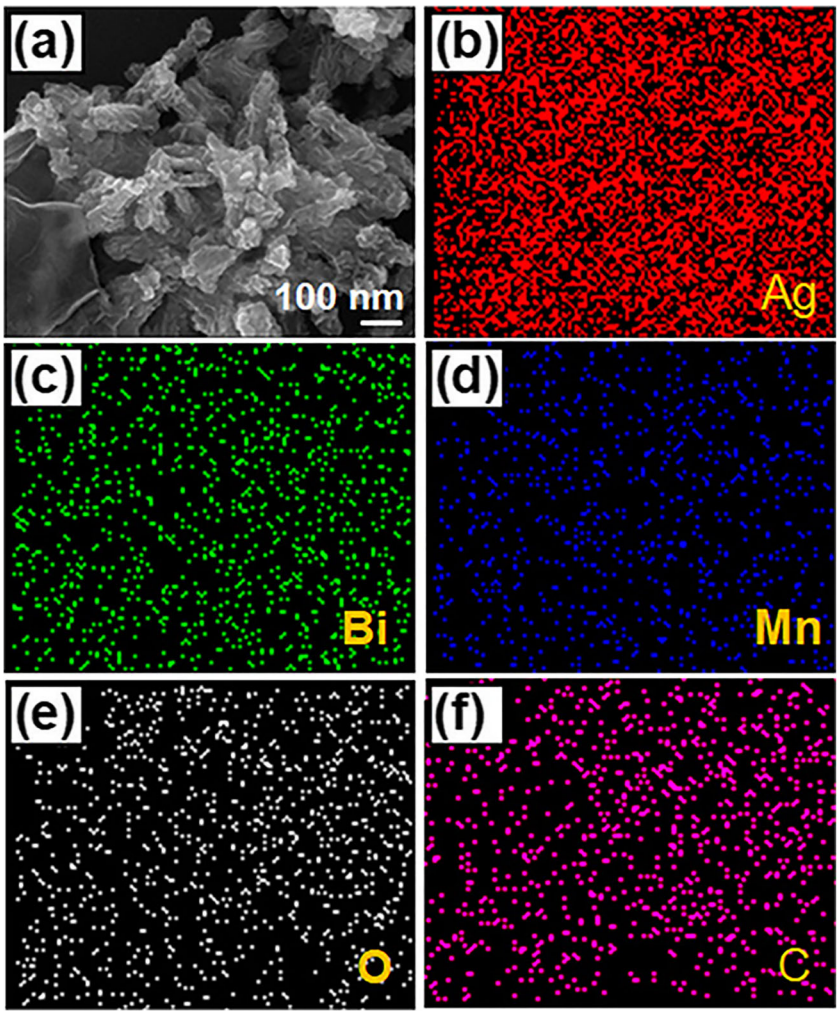

Fig. 3 **a** SEM images of 60% rGO-AM; elemental mapping images of 60% rGO-AM **b** Ag, **c** Bi, **d** Mn, **e** O, and **f** C

expected, the rod-like $Ag_4Bi_2O_5$ grows on the surface of wrinkled rGO first; afterwards, the nanoparticles are formed on the rods so as to take the shape of corncob. The catalytic activity can be greatly improved by the nanoscale composition, large specific surface area, and numerous exposed active sites.

Figure 2 displays the SEM images of the rGO and AM-rGO composite with different contents of rGO from 10 to 70%. Figure 2a indicates that rGO has a wrinkled surface which can be beneficial to enlarge its specific surface area so as to have more exposed active site to enhance the catalytic performance. It is clear that the morphology of $Ag_4Bi_2O_5/MnO_x$ is rod-like with a length of 200 nm and width of 50 nm. As shown in Fig. 2b–h, the rGO is coated by $Ag_4Bi_2O_5/MnO_x$, which is conductive to exerting the synergistic effect of $Ag_4Bi_2O_5/MnO_x$ and rGO. In addition, the special structure not only increases the specific surface area of the composite and exposes more uniform active sites but also shortens the transfer pathway for material and electron to benefit improving the catalytic performance of rGO-AM composites.

In order to realize the element distributions of rod-like $Ag_4Bi_2O_5/MnO_x$, rGO-AM with 60% rGO was examined by mapping method. As clearly displayed in Fig. 3, besides the inherent element Ag, Bi, Mn, and O, the element C is mixed in the prepared material successfully. Moreover, the Ag, Bi, Mn, O, and C elements are uniformly distributed.

EDS analysis was employed to check the chemical composition, and the results are shown in Fig. 4a. It is proved that the prepared composite contains Ag, Bi, Mn, O, and C elements, and the element C is uniformly dispersed, inferring that the rGO-AM composite has been synthesized successfully. Meanwhile, it is shown that the atomic ratio of Ag/Bi (18.56:9.26) is approximately equal to the theoretical ratio of 2:1 in the $Ag_4Bi_2O_5$, while the atomic ratio of Bi/Mn is 1.25, which is closed to the theoretical value of 1.33. Besides, atom C accounts for 1.45% [52].

Figure 4b shows the XRD patterns of the samples with different contents of 10–70% rGO. It can be seen that all samples exhibit sharply characteristic peaks at $2\theta = 26.37°$, 31.25°, 31.85°, 37.76°, 48.35°, and 56.19°, corresponding to planes of (112), (411), (312), (600), (314), and (332) of $Ag_4Bi_2O_5$, respectively. That well matches the standard card JCPDS 87-0866 of $Ag_4Bi_2O_5$. The composite containing rGO still represents the characteristic peaks of $Ag_4Bi_2O_5$, demonstrating its loading process on rGO has not affected the crystal form and the structure of nano-$Ag_4Bi_2O_5$. Meanwhile, the pattern indicates that there is no obvious peak of manganese dioxide, indicating it is a kind of amorphous MnO_x with the x value of 1–2.

Figure 5 shows the XPS results of the valence state of the elements in the as-prepared composite. Figure 5a shows the XPS spectra of elemental carbon, which present two strong peaks at 288.4 eV and 284.9 eV, indicating the

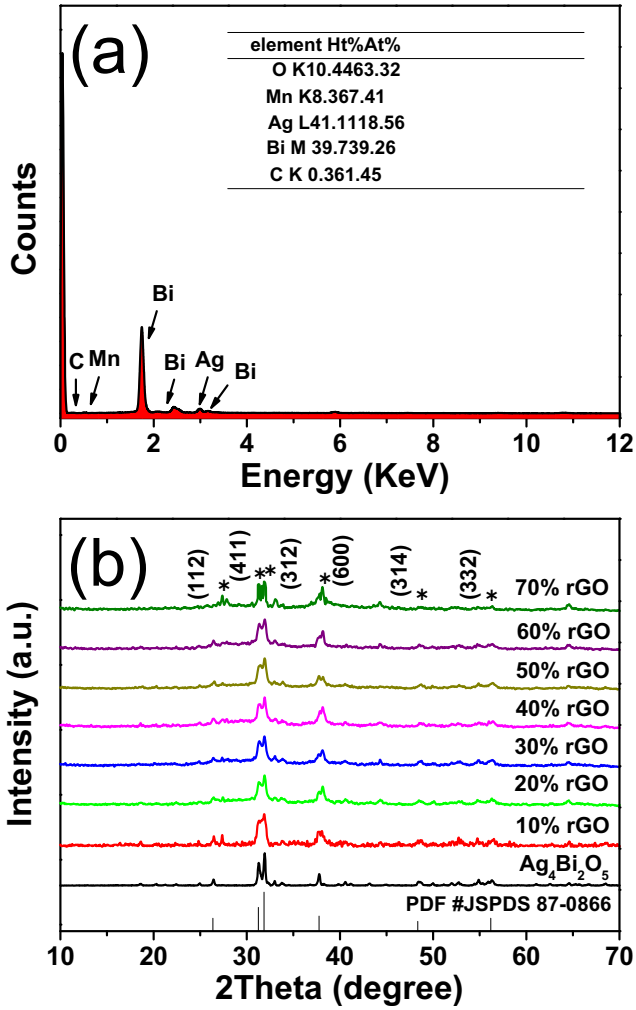

Fig. 4 **a** EDS spectra of 60% rGO-AM. **b** XRD of $Ag_4Bi_2O_5/MnO_x$/rGO with different content of rGO (0–70%)

existence of sp^2 carbon [52]. The two peaks at 368.3 eV and 374.4 eV correspond to the existence of $Ag3d_{5/2}$ and $Ag3d_{3/2}$, respectively, demonstrating element Ag exists in the valence state of + 1 (Fig. 5b) [53]. As seen from Fig. 5c, two peaks (164.0 eV and 158.7 eV) correspond to $Bi4f_{5/2}$ and $Bi4f_{7/2}$, respectively. These results prove Bi exists in the valence state of + 3 [53]. Figure 5d shows the 2p orbit of Mn in GO-AM, and the appearance of two peaks at 642.6 eV and 654.1 eV corresponding to $Mn2p_{3/2}$ and $Mn2p_{1/2}$ respectively proves the existence of Mn^{4+} [54]. In general, all the four spectra of Fig. 5 prove that the as-prepared $Ag_4Bi_2O_5/MnO_x$/rGO accords with theory and our expectation [54].

Electrocatalytic performance

Figure 6a illustrates that there is an obvious peak of oxygen reduction reaction at − 0.06 V of rGO-AM in the 0.1 M KOH saturated with O_2. linear sweep voltammetry

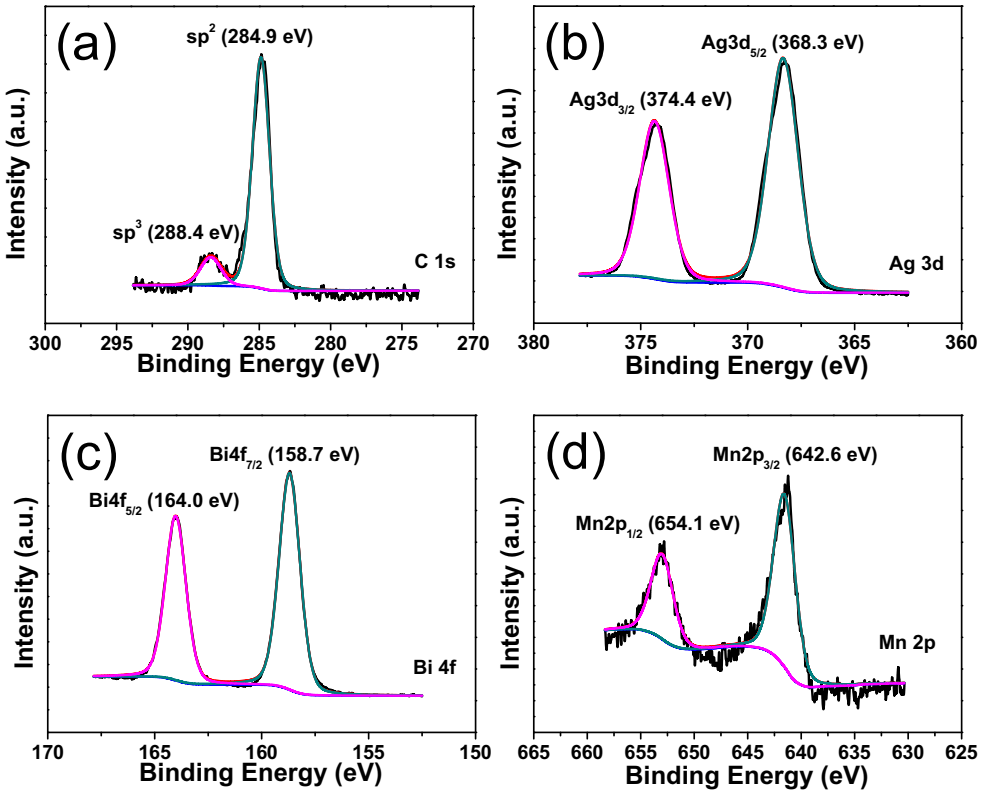

Fig. 5 X-ray photoelectron spectroscopy (XPS) spectra of 60% rGO-AM composite **a** C_{1s}, **b** Ag_{3d}, **c** Bi_{4f}, and **d** Mn_{2p}

test was conducted via rotating disk electrode (RDE) to investigate the electrocatalytic ability for ORR of the prepared composites with different contents of rGO. Figure 6b shows the LSV plots of nano-rGO-AM composites with different contents of rGO and tested at a rotating speed of 1600 rpm and a scanning rate of 5 mV s^{-1}. Based on the former research [55], the $Ag_4Bi_2O_5/MnO_x$ composite without rGO possesses the performance that the initial potential (v_o), half-wave potential ($v_{1/2}$), and limiting current density (j) are 0.089 V, − 0.046 V, and 5.51 mA cm^{-2}, respectively. With addition of 10% rGO, the initial potential and half-wave potential of the new composite become more positive value of 0.093 V and − 0.035 V respectively, together with a great limiting current density of 5.204 mA cm^{-2}. As the amount of rGO increases, $v_{1/2}$ of rGO-AM composite gradually becomes more positive, and j becomes even higher. When the content of rGO reaches 60%, the half-wave potential attains the most positive value (− 0.0419 V), the initial potential reaches 0.0799 V, and j reaches 6.164 mA cm^{-2}. Nevertheless, when the ratio of rGO is up to 70%, the half-wave potential of rGO-AM starts to become negative, meaning the synergistic effect of Ag, Bi, and Mn is weakened and the catalytic property is decreased due to an excessive amount of rGO. Table S3 exhibits the comparison of v_o, $v_{1/2}$, and j among the rGO-AMs with different contents of rGO.

Figure 6c shows the LSV plots of 60% rGO-AM composite at different rotating speeds. In consideration of the probable side reaction, all of the LSV curves have been treated by taking out the background current of the bare electrode and the curves concerning to $Ag_4Bi_2O_5$ have been taken out the part of itself (at the same speed but with Ar saturated). The related curves are shown in Figure S1. According to the analysis of separate current densities at − 0.35 V, − 0.30 V, − 0.25 V and − 0.20 V, the Koutecky–Levich curves of 60% rGO-AM are shown in Fig. 6e. The calculations showed the number of transferring electrons for ORR is 3.84, 3.76, 3.72, and 3.66 during the catalytic process, respectively, which are close to four-electron reaction, and the results are shown in Fig. 6f. The data processing was according to the following formula:

Fig. 6 (**a**) CV curves of 60% rGO-AM in O_2 and Ar-saturated 0.1 mol L^{-1} KOH, (**b**) LSV curves of rGO-AM with different ratios of rGO (10% to 70% rGO) in O2-saturated 0.1 mol L^{-1} KOH, (**c**) LSV curves of 60% rGO-AM at different rotational speeds, (**d**) Tafel curves of 60% rGO-AM and commercial Pt/C (**e**) Koutecky-Levich curves of 60% rGO-AM at different potentials, (**f**) electron transfer number of 60% rGO-AM at the corresponding potentials, (**g**) LSV curves of rGO, ABO, ABO-M, 60% rGO-AM, and commercial Pt/C, (**h**) comparison of kinetic current density j_K at −0.03V (A g^{-1}) among rGO, ABO, ABO-M and 60% rGO-AM. (LSV conditions: scan rate of 5 mV s^{-1}, rotational speed of 1600 rpm) ▶

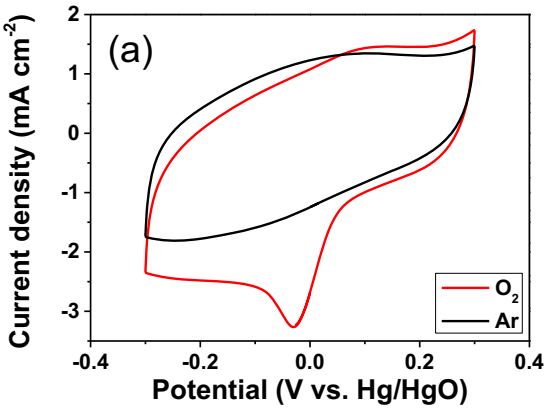
(a)
Current density (mA cm-2)
Potential (V vs. Hg/HgO)
O2
Ar

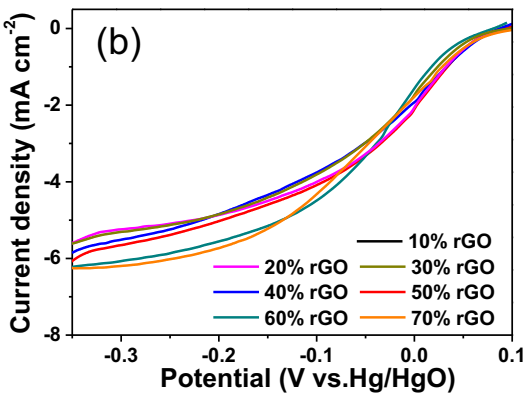
(b)
Current density (mA cm-2)
Potential (V vs.Hg/HgO)
10% rGO
20% rGO
30% rGO
40% rGO
50% rGO
60% rGO
70% rGO

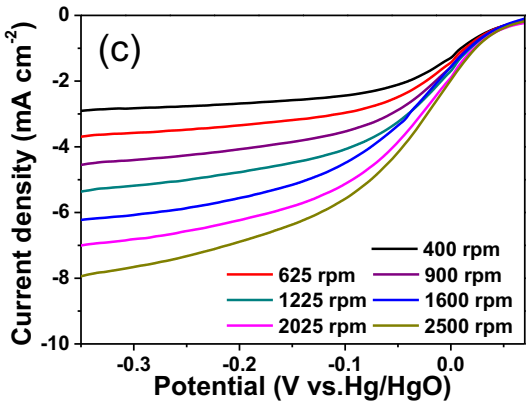
(c)
Current density (mA cm-2)
Potential (V vs.Hg/HgO)
400 rpm
625 rpm
900 rpm
1225 rpm
1600 rpm
2025 rpm
2500 rpm

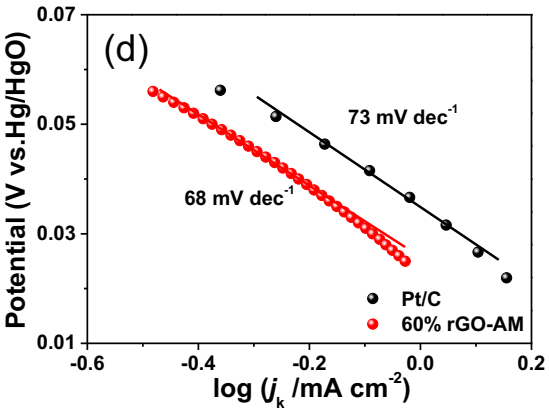
(d)
Potential (V vs.Hg/HgO)
log (jk /mA cm-2)
73 mV dec-1
68 mV dec-1
Pt/C
60% rGO-AM

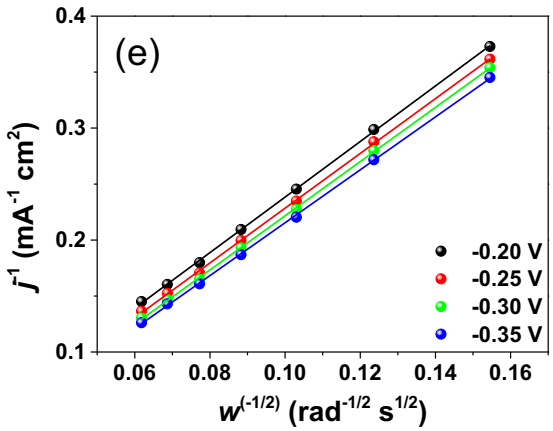
(e)
j-1 (mA-1 cm2)
w(-1/2) (rad-1/2 s1/2)
-0.20 V
-0.25 V
-0.30 V
-0.35 V

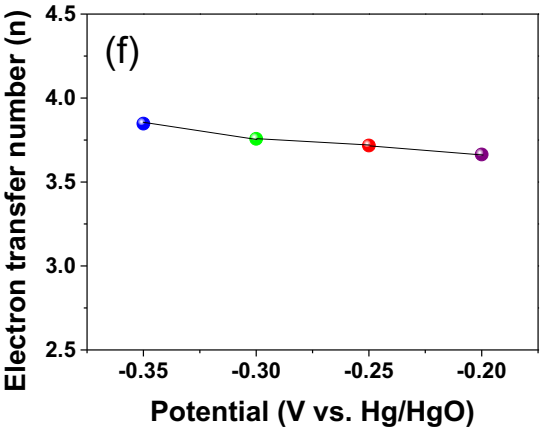
(f)
Electron transfer number (n)
Potential (V vs. Hg/HgO)

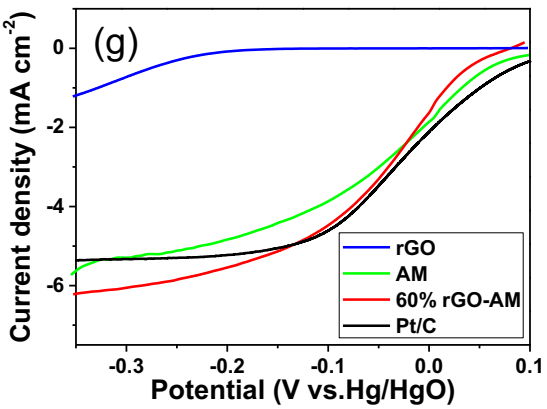
(g)
Current density (mA cm-2)
Potential (V vs.Hg/HgO)
rGO
AM
60% rGO-AM
Pt/C

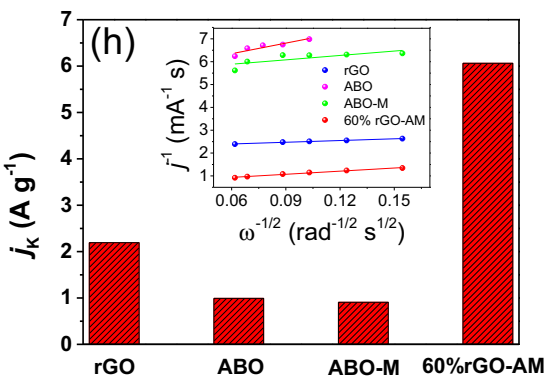
(h)
jK (A g-1)
j-1 (mA-1 s)
ω-1/2 (rad-1/2 s1/2)
rGO
ABO
ABO-M
60% rGO-AM
rGO
ABO
ABO-M
60%rGO-AM

$$\frac{1}{j}=\frac{1}{j_L}+\frac{1}{j_K}=\frac{1}{B\omega^{\frac{1}{2}}}+\frac{1}{j_K}$$

$$B=0.62nFC_0D_0^{\frac{2}{3}}V^{-\frac{1}{6}}$$

Here, j is the measured current density, j_K and j_L are the kinetic and limiting current densities, ω is the angular velocity of the disk, n is electron transfer number, F is the Faraday constant (96,500 C mol^{-1}), C_0 is the concentration of O_2 in 0.1 mol L^{-1} KOH solution (1.26×10^{-3} mol L^{-1}), D_0 is the diffusion coefficient of oxygen in 0.1 mol L^{-1} KOH solution (1.93×10^{-5} cm^2 s^{-1}), and V is the viscosity coefficient of the solution (0.1 cm^2 s^{-1}) [56].

Figure 6d shows that the Tafel slope of 60% rGO-AM is 73 mV dec^{-1}, close to that of Pt/C (68 mV dec^{-1}), demonstrating the catalytic activity of 60% rGO-AM approximates to that of commercial Pt/C [57].

As shown in Fig. 6g, the initial potential of commercial Pt/C is 0.017 V, half-wave potential is − 0.03 V, and limiting current density (at − 0.30 V) is − 5.09 mA cm^{-2}. By comparison, the half-wave potential of 60% rGO-AM is 11 mV lower than that of Pt/C, while the initial potential of 60% rGO-AM is 62 mV more positive than that of Pt/C and j is higher than that of commercial Pt/C. Figure 6h shows that the ternary catalyst possesses much huger kinetic current density (j_K) than the single and binary materials. The kinetic current density of 60% rGO-AM is 6.06 A g^{-1}, while that of the other three materials is about 1–2.2 A g^{-1}. There are three advantages of adding rGO to the $Ag_4Bi_2O_5/MnO_x$ composites: the first is to enhance the electrical conductivity of the composite; the second is to realize a synergistic effect of metallic elements Ag, Bi, and Mn to catalyze ORR process; and the last is to provide large specific surface area to improve the catalytic activity. Combined with the above observations, the $Ag_4Bi_2O_5/MnO_x$/rGO composite achieves such an outstanding ORR catalytic performance.

Figure 7a exhibits the i–t chronoamperometric curves of 60% rGO-AM and commercial Pt/C to explore their long-term stability. After the continuous test of 10,800 s, the 60% rGO-AM sample reserves about 86% of its initial performance while the commercial Pt/C undergoes a larger decay of 42% in ORR catalytic activity, which explains that the prepared material possesses greater durability as compared with Pt/C. In addition, Fig. 7b shows the methanol tolerance of Pt/C and 60% rGO-AM by adding 3.0 mol L^{-1} CH_3OH to 0.1 M KOH saturated with O_2. It can be seen that the catalytic current of Pt/C drops rapidly while the current of the as-prepared 60% rGO composite almost has no change after the adding process, which reveals 60% rGO-AM has superior methanol tolerance than that of Pt/C catalyst. These experiments prove that 60% rGO-AM is an excellent catalyst for ORR with long durability and great methanol tolerance.

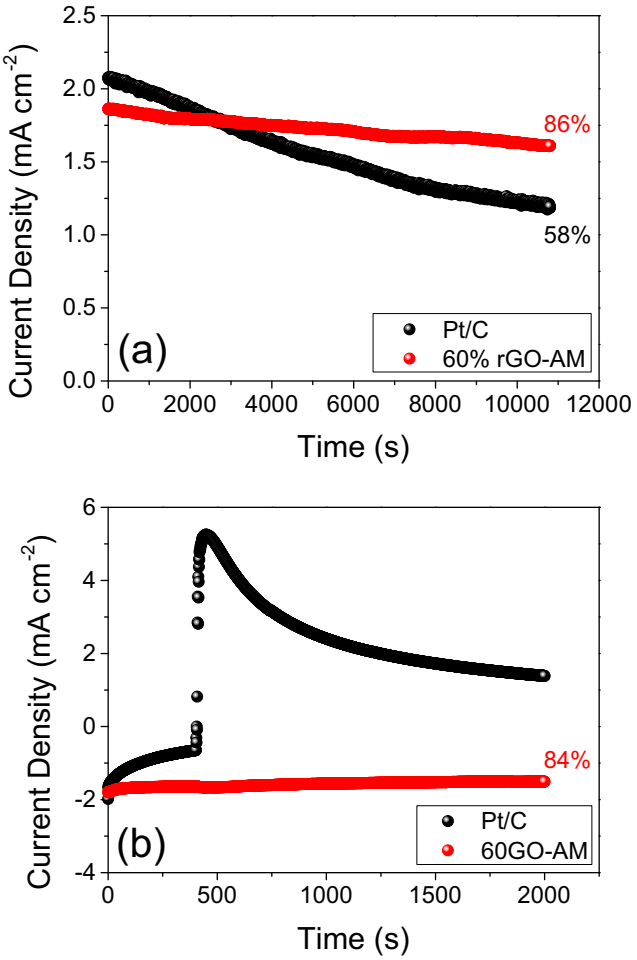

Fig. 7 **a** i–t chronoamperometric curves of 60% rGO-AM and commercial Pt/C. **b** Methanol tolerance of 60% rGO-AM and commercial Pt/C by the chronoamperometric response with adding 3.0 mol L^{-1} CH_3OH at about 400 s. (Test conditions: in O_2-saturated KOH solution, at − 0.03 V and 1600 rpm)

Furthermore, the composite was contrasted to other related catalysts, and their relevant performance parameters of ORR are listed in Table S4. It can be seen that the prepared catalyst possesses higher ORR catalytic performance than the others.

Conclusions

The rGO-AM composite was synthesized by coprecipitation on the base of rod-like nano-$Ag_4Bi_2O_5/MnO_x$. By the investigation on the content of rGO, it is found that the composite of 60% rGO exhibits the highest catalytic performance for ORR. Besides, the composite with 60% rGO displays more excellent long-term stability and methanol tolerance than that of commercial Pt/C. Its excellent ORR catalytic performance is attributed to the synergistic effect of Ag, Bi, Mn, and C. That behaves as follows: the combination of Ag and Mn increases the catalytic activity for ORR, and the synergy effect of Bi and Mn and the corncob-like structure of $Ag_4Bi_2O_5/MnO_x$

composite enhances the stability of the prepared material. In addition, the wrinkle morphology of rGO is beneficial to increase the specific surface area and conductivity of the composite so that more active sites are exposed and short transfer pathway for electron is created. Consequently, the catalytic property is improved. In conclusion, rGO-AM will be a promising high-efficient catalyst for the oxygen reduction reaction.

Funding This work was supported by the National Natural Science Foundation of China (21676022 and 21706004) and the Fundamental Research Funds for the Central Universities (BHYC1701A and XK1802-6).

References

1. Jackson A, Viswanathan V, Forman AJ (2014) Climbing the activity volcano: core-shell Ru@Pt electrocatalysts for oxygen reduction. Chemelectrochem 1(1):67–71
2. Candelaria SL, Shao Y, Zhou W, Li X, Xiao J, Zhang GJ, Wang Y, Liu J, Li JH, Cao GZ (2012) Nanostructured carbon for energy storage and conversion. Nano Energy 1(2):195–220
3. Stamenkovic VR, Strmcnik D, Lopes PP, Markovic NM (2016) Energy and fuels from electrochemical interfaces. Nat Mater 16(1):57–69
4. Yu Y, Li H, Wang HJ, Yuan XZ, Wang GJ, Pan M (2012) A review on performance degradation of proton exchange membrane fuel cells during startup and shutdown processes: causes, consequences, and mitigation strategies. J Power Sources 205:10–23
5. Jaechan R, Haeseong J, Joohyuk P, Youngshin Y, Minjoon P, Jaephil C (2018) Seed-mediated atomic-scale reconstruction of silver manganate nanoplates for oxygen reduction towards high-energy aluminum-air flow batteries. Nat Commun 9:3715
6. Shao M, Chang Q, Dodelet JP, Chenitz R (2016) Recent advances in electrocatalysts for oxygen reduction reaction. Chem Rev 116: 35–94
7. Dai L, Xue Y, Qu L, Choi HJ, Beak JB (2015) Metal-free catalysts for oxygen reduction reaction. Chem Rev 115(11):4823–4892
8. Armand M, Tarascon JM (2018) Building better batteries. Nature 451:652–657
9. Stamenkovic VR, Strmcnik D, Lopes PP, Markovic NM (2017) Energy and fuels from electrochemical interfaces. Nat Mater 16(1):57–69
10. Carrette L, Friedrich KA, Stimming U (2015) Fuel cells-fundamentals and applications. Fuel Cells 1:5–39
11. Elia GA, Marquardt K, Hoeppner K, Fantini S, Lin R, Knipping E, Peters W, Drillet JF, Passerini S, Hahn R (2016) An overview and future perspectives of aluminum batteries. Adv Mater 28(35):7564–7579
12. Osgood H, Devaguptapu SV, Xu H, Cho J, Wu G (2016) Transition metal (Fe, Co, Ni, and Mn) oxides for oxygen reduction and evolution bifunctional catalysts in alkaline media. Nano Today 11(5): 601–625
13. Shao MH, Odell JH, Choi SI, Xia YN (2013) Electrochemical surface area measurements of platinum- and palladium-based nanoparticles. Electrochem Commun 31:46–48
14. Molaabasi F, Sarparast M, Shamsipur M, Irannejad L, Moosavi-Movahedi AA, Ravandi A, Verdom BH, Ghazfar R (2018) Shape-controlled synthesis of luminescent hemoglobin capped hollow porous platinum nanoclusters and their application to catalytic oxygen reduction and cancer imaging. Sci Rep-UK 8(1):14507
15. Lima FHB, Ticianelli EA (2004) Oxygen electrocatalysis on ultrathin porous coating rotating ring/disk platinum and platinum-cobalt electrodes in alkaline media. Electrochim Acta 49(24):4091–4099
16. Wang LL, Jin XX, Fu JH, Jiang QK, Xie Y, Huang JH, Xu L (2018) Mesoporous non-noble metal electrocatalyst derived from ZIF-67 and cobalt porphyrin for the oxygen reduction in alkaline solution. J Electroanal Chem 825:65–72
17. Lv Q, Si WY, He JJ, Sun L, Zhang CF, Wang N, Yang Z, Li XD, Wang X, Deng WQ, Long YZ, Huang CS, Li YL (2018) Selectively nitrogen-doped carbon materials as superior metal-free catalysts for oxygen reduction. Nat Commun 9(1):3376
18. Pei DN, Gong L, Zhang AY, Zhang X, Chen JJ, Mu Y, Yu HQ (2015) Defective titanium dioxide single crystals exposed by high-energy {001} facets for efficient oxygen reduction. Nat Commun 6(1):8696
19. Garsany Y, Ge J, St-Pierre J, Rocheleau R, Swider-Lyons KE (2013) Standardizing thin-film rotating disk electrode measurements of the oxygen reduction activity of Pt/C. ECS Trans 58(1): 3–14
20. Higuchi E, Uchida H, Watanabe M (2005) Effect of loading level in platinum-dispersed carbon black electrocatalysts on oxygen reduction activity evaluated by rotating disk electrode. J Electroanal Chem 583(1):69–76
21. Liu M, Chen W (2013) Green synthesis of silver nanoclusters supported on carbon nanodots: enhanced photoluminescence and high catalytic activity for oxygen reduction reaction. Nanoscale 5(24): 12558–12564
22. Wang H, Yin FX, Chen BH, He XB, Lv PL, Ye CY, Liu DJ (2017) ZIF-67 incorporated with carbon derived from pomelo peels: a highly efficient bifunctional catalyst for oxygen reduction/evolution reactions. Appl Catal B 205:55–67
23. Zhong G, Liu D, Zhang J (2017) The application of ZIF-67 and its derivatives: adsorption, separation, electrochemistry and catalysts. J Mater Chem A 6:1887–1899
24. Xia DG, Liu SZ, Wang ZY, Chen G, Zhang LJ, Zhang L, Hui SQ, Zhang JJ (2008) Methanol-tolerant MoN electrocatalyst synthesized through heat treatment of molybdenum tetraphenyl porphyrin for four-electron oxygen reduction reaction. J Power Sources 177(2):296–302
25. Chisaka M, Ishihara A, Uehara N, Matsumoto M, Imai H, Ota K (2015) Nano-TaO_xN_y particles synthesized from oxy-tantalum phthalocyanine: how to prepare precursors to enhance the oxygen reduction reaction activity after ammonia pyrolysis? J Mater Chem A 3(32):16414–16418
26. Isogai S, Ohnishi R, Katayama M, Kubota J, Kim DY, Noda S, Cha D, Takanabe K, Domen K (2012) Composite of tin nanoparticles and few-walled carbon nanotubes and its application to the electrocatalytic oxygen reduction reaction. Chem-Asian J 7(2):286–289
27. Garsuch A, Yang R, Bonakdarpour A, Dahn JR (2008) The effect of boron doping into Co-C-N and Fe-C-N electrocatalysts on the oxygen reduction reaction. Electrochim Acta 53(5):2423–2429
28. Goswami C, Hazarika KK, Bharali P (2018) Transition metal oxide nanocatalysts for oxygen reduction reaction. Mater Sci Energy Technol 1:117–128
29. Lang XS, Ge F, Cai KD, Li L, Wang QS, Zhang QG (2019) A novel Mn_3O_4/MnO nano spherical transition metal compound prepared by vacuum direct current arc method as bi-functional catalyst for lithium-oxygen battery with excellent electrochemical performances. J Alloys Compd 770:451–457
30. Liu J, Jiang L, Zhang T, Jiin J, Yuan L, Sun G (2016) Activating Mn_3O_4, by morphology tailoring for oxygen reduction reaction. Electrochim Acta 205:38–44

31. Cheng F, Su Y, Liang J, Tao Z, Chen J (2014) MnO_2-based nanostructures as catalysts for electrochemical oxygen reduction in alkaline media. Chem Mater 22:898–905
32. Hazarika KK, Goswami C, Saikia H, Borah BJ, Bharali P (2018) Cubic Mn_2O_3 nanoparticles on carbon as bifunctional electrocatalyst for oxygen reduction and oxygen evolution reactions. Mol Catal 451:153–160
33. Guillaume P, Dilek KD, Mengting Q, Cyrille C, Daniel GN (2018) Oxygen reduction reaction promoted by manganese porphyrins. ACS Catal 8:671–679
34. JohnEom C, Ding YK, Carolina A, Eun JM, Steve JM (2018) Tailoring manganese oxide with atomic precision to increase surface site availability for oxygen reduction catalysis. Nat Commun 9:4034
35. Li L, Hu ZA, An N, Yang YY, Li ZM, Wu HY (2014) Facile synthesis of MnO_2/CNTs composite for supercapacitor electrodes with long cycle stability. J Phys Chem C 118(40):22865–22872
36. Klápště B, Vondrák J, Velická J (2003) MnO_x/C composites as electrode materials II. Reduction of oxygen on bifunctional catalysts based on manganese oxides. Electrochim Acta 47:2365–2369
37. Roche I, Chaînet E, Chatenet M, Vondrák J (2007) Carbon-supported manganese oxide nanoparticles as electrocatalysts for the oxygen reduction reaction (ORR) in alkaline medium: physical characterizations and ORR mechanism. J Phys Chem C 111(3): 1434–1443
38. Kostowskyj MA, Kirk DW, Thorpe SJ (2010) Ag and Ag-Mn nanowire catalysts for alkaline fuel cells. Int J Hydrog Energy 35(11):5666–5672
39. Guo J, Hsu A, Chu D, Chen R (2010) Improving oxygen reduction reaction activities on carbon-supported ag nanoparticles in alkaline solutions. J Phys Chem C 114(10):4324–4330
40. Tang Q, Jiang L, Qi J, Jiang Q, Wang S, Sun G (2011) One step synthesis of carbon-supported Ag/Mn_yO_x composites for oxygen reduction reaction in alkaline media. Appl Catal B 104(3-4):337–345
41. Lee K, Ahmed MS, Jeon S (2015) Electrochemical deposition of silver on manganese dioxide coated reduced graphene oxide for enhanced oxygen reduction reaction. J Power Sources 288:261–269
42. Xue Y, Sun S, Wang Q, Dong Z, Liu Z (2018) Transition metal oxide based oxygen reduction reaction electrocatalysts for energy conversion systems with aqueous electrolyte. J Mater Chem A 6: 1887–1899
43. Zhou M, Chen C, Du Y, Li B, Wen D, Dong S (2010) An IMP-reset gate-based reusable and self-powered "smart" logic aptasensor on a microfluidic biofuel cell. Lab Chip 10:29–32
44. Shen A, Zou Y, Wang Q, Dryfe RA, Huang X, Dou S, Dai LM, Wang SY (2014) Oxygen reduction reaction in a droplet on graphite: direct evidence that the edge is more active than the basal plane. Angew Chem Int Ed 53(40):10804–10808
45. Li Y, Zhou W, Wang H, Xie L, Liang Y, Wei F, Idrobo JC, Pennycook SJ, Dai HJ (2012) An oxygen reduction electrocatalyst based on carbon nanotubegraphene complexes. Nat Nano7:394–400
46. Chen X (2015) Graphyne nanotubes as electrocatalysts for oxygen reduction reaction: the effect of doping elements on the catalytic mechanisms. Phys Chem Chem Phys 17(43):29340–29343
47. Qiu HJ, Liu L, Wang Y (2016) Template-directed fabrication of 3D graphene-based composite and their electrochemical energy-related applications. Sci Bull 61:443–450
48. Yin H, Zhang C, Liu F, Hou Y (2014) Doped graphene: hybrid of iron nitride and nitrogen-doped graphene aerogel as synergistic catalyst for oxygen reduction reaction. Adv Funct Mater 24(20):2930–2937
49. Liang Y, Wang H, Zhou J, Li Y, Wang J, Regier T, Dai HJ (2012) Covalent hybrid of spinel manganese-cobalt oxide and graphene as advanced oxygen reduction electrocatalysts. J Am Chem Soc 134(7):3517–3523
50. Bikkarolla S, Yu F, Zhou W, Joseph P, Cumpson P, Papakonstantioun P (2014) A three-dimensional Mn_3O_4 network supported on a nitrogenated graphene electrocatalyst for efficient oxygen reduction reaction in alkaline media. J Mater Chem A 2(35):14493–14501
51. Li S, Ding L, Fan L (2015) Electrochemical synthesis of sulfur-doped graphene sheets for highly efficient oxygen reduction. Sci China Chem 58(3):417–424
52. Chen DM, Wang PY, Sun YZ, Zhu BX, Pan JQ (2017) Preparation of nano-$Ag_4Bi_2O_5$/graphene oxide composite and study of its catalytic performance for oxygen reduction reaction. Int J Electrochem Sci 12:1263–1271
53. Sun YZ, Yang M, Pan JQ, Wang PY, Li W, Wan PY (2016) Manganese dioxide-supported silver bismuthate as an efficient electrocatalyst for oxygen reduction reaction in zinc-oxygen batteries. Electrochim Acta 197:68–76
54. Guo D, Dou S, Li X, Xu JT, Wang SY, Lai LF, Liu HK, Ma JM, Dou SX (2016) Hierarchical MnO_2/rGO hybrid nanosheets as an efficient electrocatalyst for the oxygen reduction reaction. Int J Hydrog Energy 41(10):5260–5268
55. Zeng X, Pan JQ, Sun YZ (2017) Preparation of $Ag_4Bi_2O_5/MnO_2$ corn/cob like nano material as a superior catalyst for oxygen reduction reaction in alkaline solution. Catalysts 379:1–13
56. Sheng ZH, Gao HL, Bao WJ, Wang FB, Xia XH (2011) Synthesis of boron doped graphene for oxygen reduction reaction in fuel cells. J Mater Chem 22:390–395
57. Goh FWT, Liu Z, Ge X, Zong Y, Du G, Hor TSA (2013) Ag nanoparticle-modified MnO_2, nanorods catalyst for use as an air electrode in zinc-air battery. Electrochim Acta 114:598–604